Received: 15 November 2021 | Revised: 23 January 2022 | Accepted: 10 February 2022

DOI: 10.1002/app.52363

ARTICLE

Applied Polymer SCIENCE WILEY

Graphite nanosheet/polyaniline nanocomposites: Effect of in situ polymerization and dopants on the microstructure, thermal, and electrical conduction properties

Eliza Sbrogio Martin[1] | **Alex Otávio Sanches**[1] | **Thuany Garcia Maraschin**[2] | **Nara Regina de Souza Basso**[2] | **Fernando Rogério de Paula**[1] | **José Antonio Malmonge**[1]

[1]Universidade Estadual Paulista (UNESP), Faculdade de Engenharia, Câmpus de Ilha Solteira, Ilha Solteira, Brazil

[2]Escola Politécnica, Pontifícia Universidade Católica do Rio Grande do Sul (PUCRS), Porto Alegre, Brazil

Correspondence
Alex Otávio Sanches and José Antonio Malmonge, Universidade Estadual Paulista (UNESP), Faculdade de Engenharia, Câmpus de Ilha Solteira. Av. Brasil, 56, 15385-000, Ilha Solteira, SP, Brazil.
Email: alex.o.sanches@unesp.br and jose.malmonge@unesp.br

Funding information
Conselho Nacional de Desenvolvimento Científico e Tecnológico, Grant/Award Number: 309249/2015-5; Coordenação de Aperfeiçoamento de Pessoal de Nível Superior, Grant/Award Number: 001; Fundação de Amparo à Pesquisa do Estado de São Paulo, Grant/Award Number: 2013/07296-2

Abstract

This work proposed a study of in situ polymerization of polyaniline (Pani) in the presence of graphite nanosheets (GNS). The study focused on the different physical–chemical interactions promoted among them during the Pani synthesis using different dopants (HCl and DBSA). By means of Fourier transform infrared spectroscopy (FTIR), scanning electron microscopy (SEM), X-ray diffraction (XRD), thermogravimetry (TG/DTG), and DC electrical conductivity, the study demonstrated the production of nanocomposites with different electrical, thermal, and morphological properties and correlating them with the different physico-chemical interactions evidenced from the different dopants used. The type of anchoring has been shown to directly influence the amount of GNS that could be incorporated into the reaction medium. It also demonstrated as highlight the possible existence of a hybrid intercalation/pseudo-intercalation process that was responsible for promoting an increase of up to 50°C in the thermal stability of the nanocomposites depending on the general characteristics of the synthesized Pani type. The electrical conductivity of the nanocomposites proved to be dependent on the type of dopant, the GNS/Pani interaction, and the regularity of the Pani coating on the nanostructure surface, resulting in a non-universal percolation profile.

KEYWORDS
graphite nanosheets, nanocomposite, polyaniline

1 | INTRODUCTION

Due to promising battery applications,[1–5] electromagnetic shielding,[6–9] actuators,[10–13] energy storage systems,[14–21] and other functional applications,[22–29] the study and development of composites and nanocomposites using intrinsically conducting polymers (ICP) as a matrix and some carbon allotropes, such as graphite,[12,13,27,28] graphene,[2,5,7,18,20] carbon black,[3,30,31] fullerenes,[19,32] and carbon nanotubes,[4,29,33–35] has been intensifying in the literature. The function of ICP is to improve the contact between the particles or nanoparticles of inclusion, creating a three-dimensional network of conduction in the material.[36]

Several groups have reported the production of functional nanocomposites with ICP and graphite nanosheets (GNS) as an alternative to a high-volume fraction of graphite or expanded graphite (EG) needed to produce

composites with high conductivity values.[37–41] Such a fact is possible due to the high aspect ratio obtained for such materials through the ultrasonic exfoliation of the chemically expanded graphite.

The advantage of using GNS is that your production is extremely simpler and much cheaper than producing graphene, there being, as in the case of the study, the possibility of producing the material in its dry state. In addition to these factors, GNS are widely studied due to their greater ease of dispersion and less agglomeration than graphene in different matrices. Among the conductive polymers employed, Pani stands out for its ease of synthesis, environmental stability, redox reversibility, and high electrical conductivity in its doped state.[37] One of the most commonly used techniques for producing such functional materials with Pani is the oxidative polymerization of aniline (An) in situ in the presence of GNS. This method is reported to produce nanocomposites with excellent filler dispersion and strong connections between the matrix and the filler.[42] One of the major problems encountered in such a production technique is its high dependence on several physical–chemical factors, such as the type of dopant used, hydrophobicity of the anchoring medium, pH of the initial reaction solution, order of reagent mixing, temperature, volumetric quantity, and type of surface of the anchoring medium.[43] These are factors that are not yet fully understood and that directly interfere in the type of Pani interaction synthesized with the GNS and, therefore, in its final properties.[43] In view of this panorama, this work aimed to study in situ polymerization of Pani in the presence of GNS, focusing on the different physical–chemical interactions promoted between them using different dopants (HCl and DBSA). The study demonstrated that, depending on the dopant characteristics, the aniline monomer anchoring process in the GNS results in a different morphological structure and intercalation/pseudo-intercalation process. Such factors were also found to be decisive in terms of the amount of GNS that can be incorporated into the reaction medium.

2 | MATERIALS AND METHODS

2.1 | Materials

Sufuric acid (98%) and nitric acid (65%) were purchased from Química Moderna and used as received. Natural graphite in flake form (332461) was provided by Sigma-Aldrich. Ammonium peroxydisulfate (APS), dodecylbenzenesulfonic acid (DBSA-70%), and aniline, distilled under vacuum, were purchased from Sigma-Aldrich. Hydrochloric acid P.A was purchased from Synth.

2.2 | Synthesis of GNS

The GNS were prepared according to the methodology described by Fim.[44] For this, 2 g of natural graphite flake was added to a mixture of 24 mL of H_2SO_4 and 6 mL of HNO_3. The mixture was stirred at room temperature for 24 h. Then, it was washed with distilled water until a neutral pH was achieved and dried in an oven at 100°C for a period of 3 h to obtain the intercalated graphite. The intercalated graphite was subsequently expanded in a preheated oven (Jung oven, model 3012) at a temperature of 1000°C for 30 s to obtain expanded graphite particles with micron dimensions. To obtain the GNS, the expanded graphite was immersed in a 70% alcoholic solution and placed in an ultrasound bath (Maxiclean 1450-Unique) for 9 h. The resulting dispersion was filtered through a sintered funnel (G2), and the resulting solid was placed in a preheated oven for 3 h at 100°C.

2.3 | Synthesis of Pani-DBSA and Pani-HCl

For the synthesis of nanocomposites, two types of dopant acids were chosen for study: HCl and DBSA. HCl is a strong acid, has small molecule and is commonly used in polyaniline synthesis. In turn, DBSA is a large molecule that acts as a surfactant and dopant, which could assist in the dispersion of GNS.

Pani-DBSA samples were obtained by oxidative polymerization of aniline in an aqueous solution using DBSA as a doping agent. Ammonium persulfate was used as an oxidizing agent. The proportion between the reagents used followed the molar ratio of 1:1.5:1 of aniline, APS, and DBSA, respectively. For this, in a 250 mL beaker, 3.1 mL of DBSA was dispersed in 35 mL of water under mechanical stirring at 700 rpm for 30 min at 5°C. Then, 0.6 mL of An was added slowly to the dispersion, which remained under the same stirring conditions and temperature for an additional 1 h. After this period, an aqueous solution of APS (2.3 g of APS in 10 mL of distilled water) was added in one step to the mixture. The system was kept under stirring for another 5 min, and thereafter, the reaction was kept at rest at 5°C for 12 h for total polymerization. Pani-DBSA was then precipitated with acetone and filtered under vacuum in a Büchner funnel and washed alternately with distilled water and acetone several times. The precipitate was dried in an oven at 60°C for 24 h and then stored in a closed container for further characterization.

In turn, the synthesis of Pani-HCl followed a similar process and molar ratios to that described for Pani-DBSA; however, an aqueous HCl solution was used as a reaction

medium. In this, 1 mL of An was dispersed under stirring in 60 mL of a 1 mol L^{-1} HCl aqueous solution. The system remained under agitation for 1 h at 5°C. Afterwards, 10 mL of an APS aqueous solution (3.8 g of APS in 10 mL of 1 mol L^{-1} HCl aqueous solution) was added to the stirring mixture in a single step. The mixture was stirred for another 5 min. Then, the system was kept at rest at 5°C for approximately 12 h. At the end of the rest period, the Pani-HCl was precipitated with acetone, filtered under vacuum in a Büchner funnel, and the precipitate was washed alternately with a 1 mol L^{-1} HCl aqueous solution and acetone several times. As in the previous case, the precipitate was dried in an oven at 60°C for approximately 24 h and then stored in a closed container for further characterization.

2.4 | Synthesis of GNS/Pani nanocomposites

GNS/Pani-HCl (PHN) and GNS/Pani-DBSA (PDN) nanocomposites were obtained by in situ polymerization of An using HCl or DBSA as a dopant and in the presence of GNS in the reaction medium. In all syntheses, the 1: 1.5: 1 molar ratio of An, APS, and HCl or DBSA, respectively, remained fixed. The variations in the mass ratios of GNS in relation to the aniline studied are shown in Table 1. In both cases studied, the different mass ratios were determined based on the construction of the percolation curve illustrated in the results of this study. The different routes for obtaining the nanocomposites are described below.

2.4.1 | Synthesis of PHN nanocomposites

Initially, the GNS were dispersed in 60 mL of a 1 mol L^{-1} HCl aqueous solution. The dispersion was mechanically stirred for 10 min and then placed in an ultrasound bath for 2 h. After this period, it was again stirred for 30 min at 5°C, and then 1 mL of An was added slowly to the stirring solution. The dispersion was stirred under the conditions described for an additional 1 h. Afterwards, the aqueous dispersion of the APS solution (3.8 g of APS in 10 mL of distilled water) was added to the stirring solution, initiating the polymerization. The mixture was stirred for another 5 min, and then the system was kept at rest at 5°C for 12 h. After the resting period, the nanocomposites were precipitated with acetone, filtered under vacuum in a Büchner funnel, and the precipitate was washed alternately with a 1 mol L^{-1} HCl aqueous solution and acetone several times. The precipitate was dried in an oven at 60°C for 24 h and stored in a closed container for further characterization.

2.4.2 | Synthesis of PDN nanocomposites

To obtain the PDN nanocomposites, first, the DBSA aqueous solution was prepared. The amount of water for dissolving the DBSA varied from 35 to 50 mL according to the amount of GNS that was used. Then, the GNS was added to the DBSA solution while stirring. The dispersion was kept under stirring for 10 min. Subsequently, this was subjected to an ultrasound bath for 2 h, followed by mechanical agitation (at 700 rpm and 5°C) for 30 min. An was then added slowly to the dispersion, which remained under the same stirring and temperature conditions for another hour. To start the polymerization reaction, the aqueous APS solution was added in a single step to the stirring dispersion. The stirring process was maintained for 5 min, and then the system was left to rest at 5°C for approximately 12 h. The PDN nanocomposites were precipitated with acetone, filtered under vacuum, and the precipitate was washed with distilled water and acetone

TABLE 1 Nanocomposite composition and nomenclature

	An: APS: HCl			
Nanocomposites	**An**	**APS**	**HCl**	**% GNS/An (m/m)**
PHN60	1.0	1.5	1.0	60
PHN100	1.0	1.5	1.0	100
PHN140	1.0	1.5	1.0	140
PHN200	1.0	1.5	1.0	200
PHN250	1.0	1.5	1.0	250
	An: APS: DBSA			
Nanocomposites	**An**	**APS**	**DBSA**	**% GNS/An (m/m)**
PDN40	1.0	1.5	1.0	40
PDN60	1.0	1.5	1.0	60
PDN80	1.0	1.5	1.0	80
PDN100	1.0	1.5	1.0	100
PDN140	1.0	1.5	1.0	140
PDN200	1.0	1.5	1.0	200
PDN250	1.0	1.5	1.0	250
PDN300	1.0	1.5	1.0	300
PDN400	1.0	1.5	1.0	400
PDN500	1.0	1.5	1.0	500
PDN600	1.0	1.5	1.0	600
PDN750	1.0	1.5	1.0	750
PDN950	1.0	1.5	1.0	950

alternately several times. After washing, the process previously described for PHN nanocomposites was followed.

2.5 | Characterization

The morphological analysis was performed using a ZEISS scanning electron microscope model EVO LS15. For this, the powder samples were fixed to an aluminum sample holder with the aid of double-sided carbon tape and metallized with a thin layer of gold.

Fourier transform infrared spectroscopy (FTIR) measurements were performed using a Nicolet Nexus 670 FT-IR spectrophotometer. KBr/sample pellets in the proportion 200/1 were prepared, and the measurements were carried out in transmittance mode. The measurements were carried out in a range of 4000–400 cm^{-1} with a resolution of 4 cm^{-1} using 128 scans.

DC electrical conductivity measurements were performed on samples pellets using the four-point method. The pellets were prepared from the particulate using a circular pellet maker subjected to 225 MPA for 15 min at room temperature. A Keithley programmable voltage and current source (236 source measure unit) and an HP model 344014 voltmeter were used. All measurements were performed at room temperature (~ 28°C). The tests were conducted in triplicate, and each pellet was subjected to a total of 20 measurements at different points on the surface pellet, with 10 measurements being made on each face (top/bottom). From the data specified for the set of 3 pellets, the mean value and standard deviation for each composition were determined.

X-ray diffraction measurements were performed on a Shimadzu XRD-6000 diffractometer with Cu–Kα radiation (wavelength of 1.5418°Å) in a range of $2\theta = 5°–60°$ at a scan rate of $1°min^{-1}$.

The thermal stability of the nanocomposites was studied by means of thermogravimetric analysis (TG/DTG). For this purpose, an SDT model Q 600 from TA instruments was used. The analysis was carried out in the temperature range between 25 and 700°C with a heating rate of 10°C min^{-1} in a dynamic nitrogen atmosphere. For each measurement, 10 mg of sample was used. Alumina crucibles were used for all measurements.

3 | RESULTS AND DISCUSSION

3.1 | Fourier transform infrared spectroscopy

FT-IR spectroscopy was used to elucidate the nature of the interactions between the different types of synthesized Pani and the GNS. Figures 1 and 2 illustrates the infrared spectra obtained for GNS, Pani-HCl, and Pani-DBSA, as well as for the nanocomposites, with emphasis on the main absorption bands in the region of interest between 2000 and 400 cm^{-1}.

The GNS showed a characteristic absorption band centered at 1633 cm^{-1}, assigned to the C=C stretching of the aromatic graphene rings.[45] The band centered at 1385 cm^{-1} was attributed to the OH stretching vibration of the carboxyl, while the band at 1105 cm^{-1} is due to the C—O stretching of C—O—C or C—OH groups from chemical groups resulting from the chemical process of oxidation of natural graphite that were not totally degraded during the heat treatment.[40,46]

Pani-HCl showed typical absorptions of its emeraldine salt form, with bands at 1562 cm^{-1} and 1477 cm^{-1} attributed to the C=C stretching deformation of quinoid rings and benzenoid rings, respectively.[47,48] The absorption at 1300 cm^{-1} was attributed to the π electron delocalization induced in the polymer due to protonation or C—N stretching of the secondary aromatic amine.[47–51] The characteristic band of the protonated Pani was observed at 1244 cm^{-1}, which is attributed to the C—N^+ stretching vibration of the polaronic structure,[47,50,52] and the band centered on 1141 cm^{-1} was attributed to the vibration mode of —NH^+= that is formed during protonation.[47,50,51]

It was also possible to verify, in the spectrum of Pani-HCl, the presence of absorption bands centered on 804 cm^{-1} and 881 cm^{-1} corresponding to the C—H outside the plane deformation of the 1,4-disubstituted benzene rings.[47,51]

In the PHN nanocomposites, it was possible to verify the presence of Pani-HCl in its doped form through the bands at 1562, 1477, and 1244 cm^{-1}. The displacement of the absorption band at 1633 cm^{-1}, associated with GNS, towards larger wave numbers as well as the displacement of the bands centered at 1562 cm^{-1} and 1477 cm^{-1}, assigned to Pani-HCl in the nanocomposites, were observed (Table 2). Such behavior indicates the possible existence of π-type bonds between the aromatic rings of the GNS with the benzenoid rings and quinoids of the Pani-HCl.[53,54] These interactions were also verified through the band displacement at 1141 cm^{-1} towards smaller wavenumbers in the PHN nanocomposites, which is related to the increase in the effective degree of delocalization that occurs due to the interactions of the π-type interactions of Pani-HCl with GNS.[53]

It was possible to observe, in all spectra of the PHN nanocomposites, the presence of the absorption band at 1400 cm^{-1}. The same band can be observed in the Pani-HCl spectrum at a low intensity. This can be attributed to both the C—N stretching of aromatic amines in the QB_tQ environment, where B_t represents the trans-benzoid

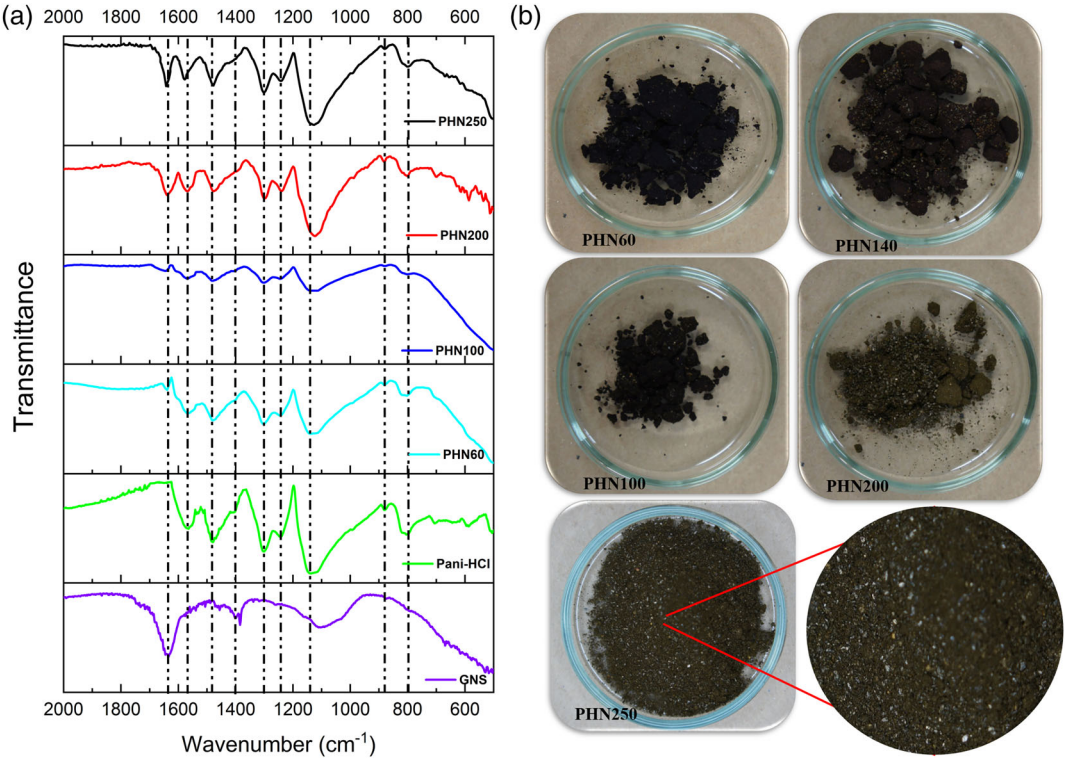

FIGURE 1 Left: (a) Fourier transform infrared (FTIR) spectra of Pani-HCl, GNS, and nanocomposites highlighting the main vibrational bands. Right: (b) Digital images of PHN nanocomposites after the final synthesis process [Color figure can be viewed at wileyonlinelibrary.com]

unit,[55–58] due to the presence of oligomers, such as phenazine units, arising from the synthesis process.[43,59–63] The digital images presented in Figure 1 indicate a color change in the nanocomposites from green to yellow/brown for the GNS concentration of 140% m/m. This change indicates the predominance of absorption processes from oligomeric units, such as phenazine-like structures formed due to ortho-coupling, induced by the increased amount of GNS in the synthesis process. Thus, this explains the greater definition of this band in the nanocomposites with a higher concentration of GNS.

Pani-DBSA (Figure 2), in its emeraldine salt form, showed absorption bands at 1540 cm^{-1} and 1465 cm^{-1}, which are related to the C=C stretching vibration of the quinoid and benzenoid rings, respectively,[64] while the 1292 cm^{-1} band was attributed to the C—N stretching vibration of the aromatic secondary amine.[64,65] Other bands correlated to the Pani-DBSA emeraldine salt form were observed at 1213 cm^{-1} (C—N^+ stretching vibration of the polaron structure) and 1101 cm^{-1}, attributed to the deformation in the plane of the C-H bond (N = Q = N, Q = NH^+-B, and B-NH^+-B mode).[55,64,65] The bands at 1030, 1003, and 877 cm^{-1} were associated with the S=O stretching vibration of the sulfonic acid groups present in the DBSA molecule, the >C—H stretching of DBSA benzene rings, and the C—H deformation outside the plane of the aromatic rings, respectively.[55,64–66] Table 2 summarizes the main absorption bands found in the aforementioned samples.The PDN nanocomposites showed the Pani-DBSA characteristic bands at 1540, 1465, 1400, 1292, 1213, and 1100 cm^{-1}. As in the PHN nanocomposites, the displacement of the band associated with GNS at 1633 cm^{-1} towards higher wavenumbers was verified, indicating a possible π-conjugated bond of the GNS structure and Pani-DBSA. This fact was also corroborated by the shift to greater wavenumbers of the absorption bands associated with the C=C stretching vibration of the Pani-DBSA quinoid and benzenoid rings at 1540 cm^{-1} and 1465 cm^{-1}, respectively. The displacement of the band at 1030 cm^{-1}, attributed to the S=O stretching vibration of the DBSA, towards higher wavenumbers suggests the performance of the GNS as anchoring bridges for the hydrophobic part of the DBSA.

The absorption band centered on 1400 cm^{-1} could also be seen in the spectra of the PDN nanocomposites. This was associated with the predominance of C—N vibrations of aromatic amines in the QB_tQ enviroment as well as the C—H in plane bending vibration of the dodecyl chain for DBSA.[67] The reduction in intensity of this band as well as

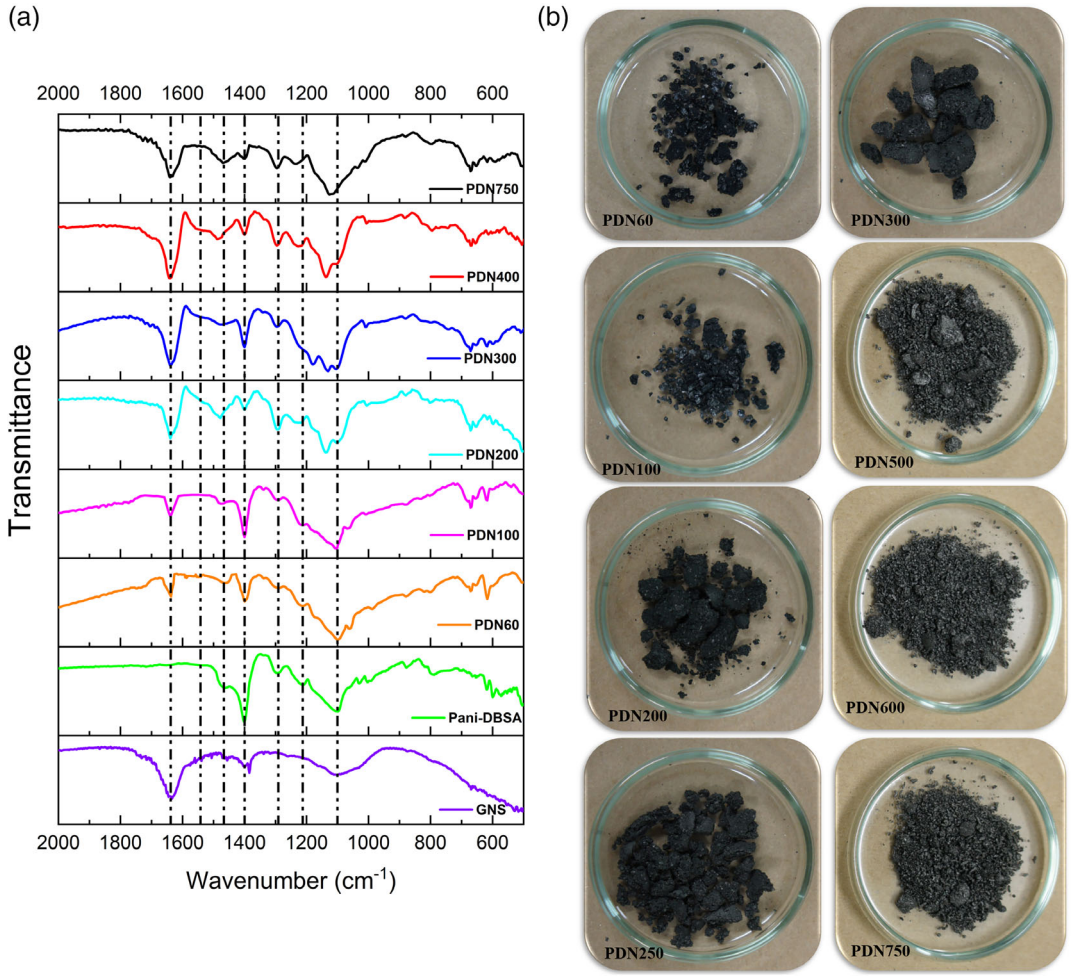

FIGURE 2 Left: (a) Fourier transform infrared (FTIR) spectra of Pani-DBSA, GNS, and nanocomposites highlighting the main vibrational bands. Right: (b) Digital images of the PDN nanocomposites after the final synthesis process [Color figure can be viewed at wileyonlinelibrary.com]

its widening with the increase in GNS content (Figure 2) is probably due to the increase in oligomeric units, such as phenazine units. However, this effect seems to be less intense in the case of PDN nanocomposites given there was no noticeable change in the color of the final synthesized material (Figure 2). In an aqueous solution, the DBSA hydrophobic segment interacts with the GNS, whereas the DBSA SO_3^- functional group interacts electrostatically with the aniline cation.[65,68,69] Thus, DBSA molecules adhered to the surface of the GNS act as bridges/nucleation sites for Pani/An.

3.2 | Morphology of the GNS/Pani nanocomposites

SEM images of the GNS are shown in Figure 3c–d. Note that they have different sizes and a fairly smooth surface and maintain their lamellar morphology.

The Pani morphology was influenced by the dopant used in the synthesis, as shown in Figures 4 and 5. A globular morphology with diameters between 80 and 200 nm was observed when using HCl as the dopant (Figure 4), whereas Pani-DBSA exhibited a disordered nanofibrillar morphology with diameters between 200 and 280 nm that aggregated into large clusters (Figure 5). Figures 4 and 5 also show representative nanocomposite SEM images that illustrate the appearance of rough structures on the smooth surface of the GNS, indicating that there was polymerization of aniline on them. The Pani distribution on the GNS surface was irregular in both cases. This irregularity increased as the GNS concentration in the reaction medium increased. However, distinctions were observed in relation to this, while the distribution of Pani-HCl occurred in islands structures, Pani-DBSA had a more uniform coating of nanosheets compared to the PHN composites. In the same way, significant changes in the Pani morphological

TABLE 2 Main vibration bands and their respective vibrational modes verified in the FTIR spectra of Pani-HCl, Pani-DBSA, and nanocomposites

	PANI-HCl Absorption (cm^{-1})					
Assignments	**GNS**	**Pani-HCl**	**PHN60**	**PHN100**	**PHN200**	**PHN250**
Stretching C=C of the quinoid rings	–	1562	1566	1569	1570	1578
Stretching C=C of the benzoid rings	–	1477	1479	1482	1478	1478
C—N stretching of secondary aromatic amine	–	1300	1304	1304	1300	1300
C—N^+ stretching of the polaronic structure	–	1244	1246	1246	1238	1242
vibration mode of —NH^+ =	–	1141	1138	1140	1130	1130
C—H outside the plane deformation of the 1,4-disubstituted benzene rings	–	881	879	879	879	879
C—H outside the plane deformation of the 1,4-disubstituted benzene rings	–	804	802	802	798	798
C=C stretching vibration of graphene rings	1633	–	1639	1642	1640	1642

	PANI-DBSA Absorption (cm^{-1})							
Assignments	**GNS**	**Pani-DBSA**	**PDN60**	**PDN100**	**PDN200**	**PDN300**	**PDN400**	**PDN750**
Stretching C=C of the quinoid rings	–	1540	1548	1546	1533	1558	1558	1504
Stretching C=C of the benzoid rings	–	1465	1464	1476	1477	1473	1489	1469
C—N stretching of secondary aromatic amine	–	1292	1288	1292	1292	1296	1296	1296
C—N^+ stretching vibration of polaron structure	–	1213	1211	1211	1227	1180	1226	1234
deformation in the plane of C—H bond (N = Q = N, Q = NH^+-B, and B-NH^+-B mode)	–	1100	1101	1103	1137	1130	1138	1126
S=O stretching vibration-sulfonic acid groups	–	1030	1060	1068	1103	1103	1103	1033
stretching of DBSA benzene rings	–	1003	988	1006	1007	1010	1007	1009
C—H deformation outside the plane of the aromatic rings	–	877	879	879	879	879	883	879
C=C stretching vibration of graphene rings	1633	–	1637	1639	1639	1639	1639	1639

structure were observed when it was synthesized in the presence of GNS. In the nanocomposites, Pani-HCl (Figure 4) showed rodlike structures, whereas Pani-DBSA (Figure 5) maintained a nanofibrillar morphology. It was also observed that the Pani-DBSA nanofibrils in the nanocomposites were more elongated and had better directional organization. The nanofibril diameters were estimated to be between 70 and 280 nm. The observed morphological difference for Pani in the nanocomposites was associated with the different interactions that exist among aniline, the GNS, the dopant, and Pani in the chemical synthesis, as exemplified by the FTIR measurements. In the synthesis of the PHN nanocomposites, the aniline cations are responsible for interacting with the GNS, being present both on the surface of the GNS and interposing inside the layers of the GNS. These are responsible for Pani nucleating from the in-situ polymerization process with the introduction of APS. In this way, the system polymerizes with a globular morphology as well as Pani-HCl. However, its growth occurs by the joining of one or more nearby nanostructures and/or by the chemical or physical interaction existing between the polymerized Pani in the reaction medium, thus assuming a rodlike structure. For PDN nanocomposites, the chemical structure of DBSA ensures that the hydrophobic part interacts directly with the GNS surface, as verified in the FTIR measurements, and the hydrophilic part interacts electrostatically with the aniline. This structure therefore functions as a nucleation site for the Pani-DBSA, ensuring the nanofibrillar morphological structure. Thus, the GNS acted as a support material that could provide a

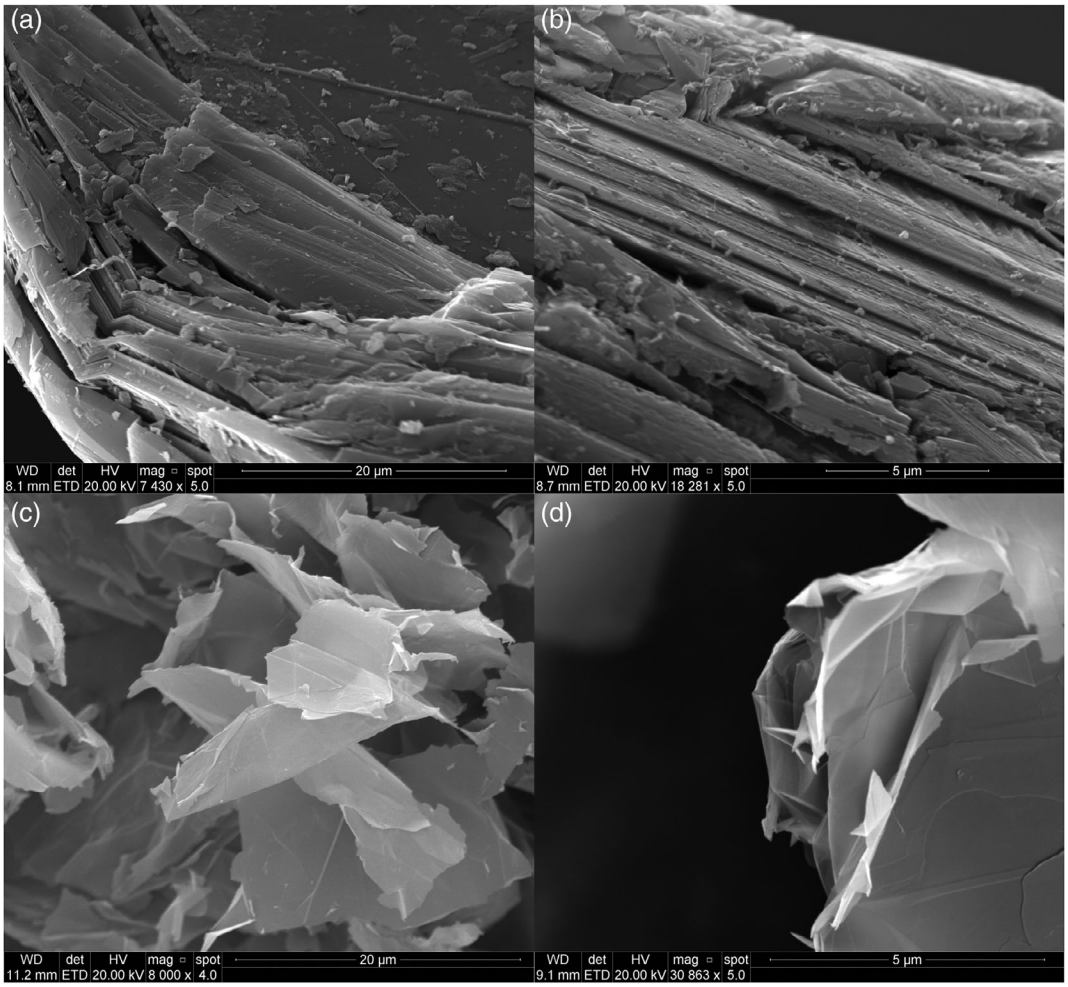

FIGURE 3 SEM images obtained from natural graphite flake (a, b) and GNS (c, d) at different scales

large number of active sites for nucleation and/or structured growth of Pani, promoting the coating of the GNS as well as the organizational change, as observed in the SEM images.

3.3 | X-ray diffraction

Figures 6 and 7 shows the X-ray diffraction patterns of GNS, Pani-HCl, Pani-DBSA, and the nanocomposites for different GNS content. The GNS diffractogram shows diffraction peaks at $2\theta = 26.45°$ and 54.28° corresponding to the planes 002 and 110, respectively.[70]

Pani-HCl (inset in Figure 6) showed crystalline peaks at $2\theta = 15°$, 20.3°, 25.2°, and 26.2° corresponding to the planes (011), (020), (200), and (121), respectively.[49,71] In turn, Pani-DBSA (inset Figure 7) exhibited diffraction patterns in $2\theta = 18.40°$, 19.30°, 24.02°, 25.4°, 26.7°, 26.9°, 30.86°, 33.32°, 37.82°, and 44.1°. In particular, the diffraction peaks observed at 19.3° and 25.4° correspond to the planes (001) and (110) representing the parallel and perpendicular periodicity, respectively, in relation to the chain axis, confirming the formation of Pani in its emeraldine salt.[64,71,72] For the nanocomposites PHN and PDN, the pattern shows a sharp peak around $2\theta = 26°$, and its intensity increases with an increase in the graphite content. Figure 8 illustrates the GNS interplanar distance in the PHN and PDN nanocomposites. It was possible to observe an expansion of the (002) GNS planes with the increase of nanoparticles content in the nanocomposites. Pani intercalation and pseudo-intercalation in GNS have been considered by many authors and there is no consensus on which of the two hypotheses prevails.[73–78] Intercalation processes occur by introducing a variety of small molecules between the graphite planes, allowing their expansion and significantly altering their electronic properties. However, the size of macromolecules, such as Pani, would contrast with the dimensions of the GNS interplanar spacing. Pseudo-intercalation processes occur by Pani interposition between the GNS. In this case, Pani would act as an element to promote a long-range order in the material, in addition to its acceptor role, facilitating

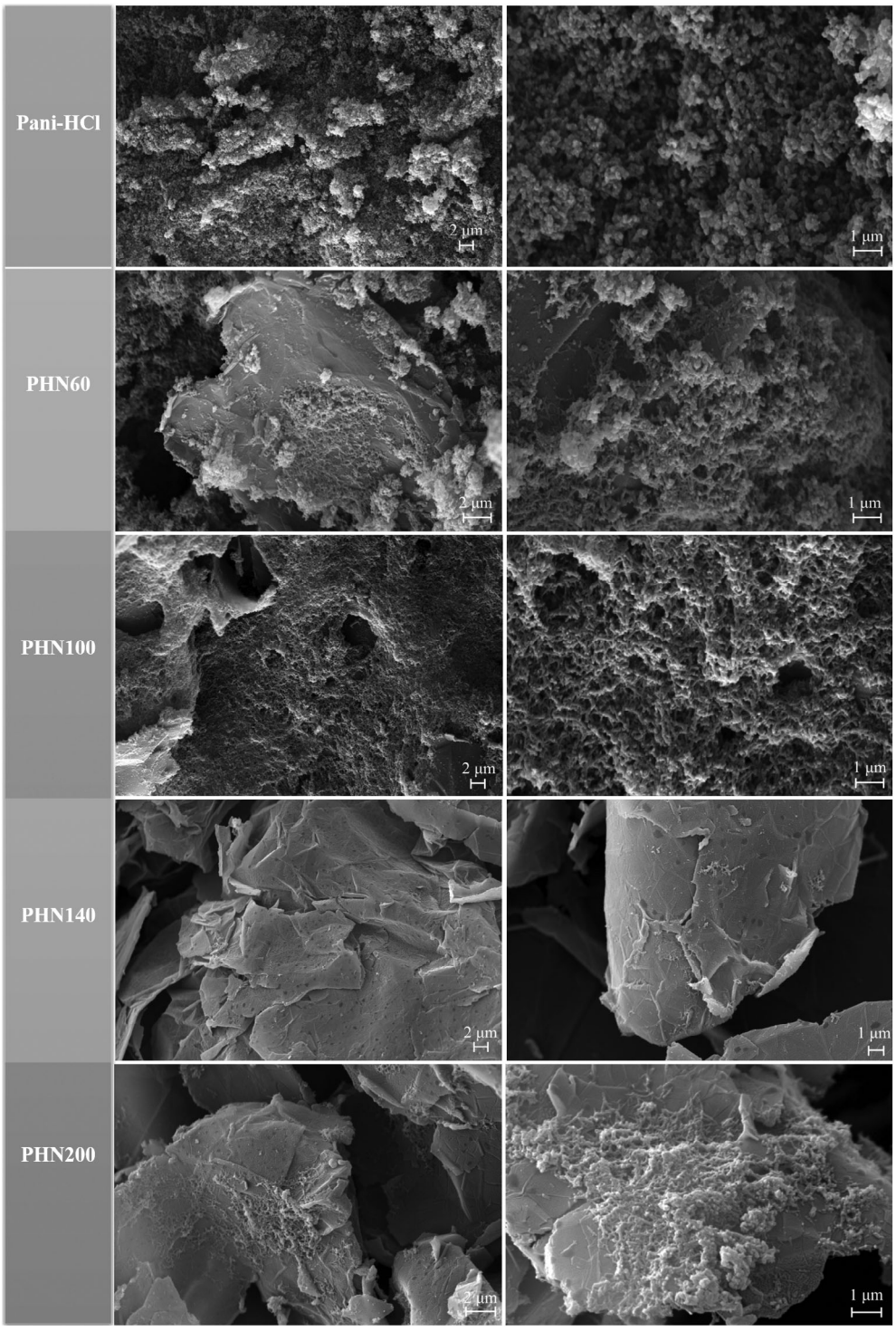

FIGURE 4 SEM micrographs obtained from Pani-HCl and nanocomposites, focusing on the morphological structure and distribution of Pani-HCl on the surface of the GNS

charge transfer processes between the GNS. Thus, Pani tends to influence the crystalline nature of graphite by means of greater relaxation of the atomic positions of the graphene, promoting an increase in the interplanar spacing of the graphite as well as a possible increase in its crystallinity in some cases.[76,78,79]

It was observed that an increase in the interplanar spacing in the nanocomposites occurred more intensely for the PHN composites, while for the PDN nanocomposites, a saturation was found above the fraction of 400% m/m of GNS. A similar effect was reported by Saini et al.[75] in Pani-DBSA/graphite composites. Interestingly, for the samples of PDN at GNS concentrations above 400% m/m, a significant increase in the intensity of the diffraction peaks corresponding to the plane (002) was also verified, demonstrating a greater crystallinity of the GNS. Thus, we propose in this work the possible occurrence of a hybrid process of intercalation and pseudo-

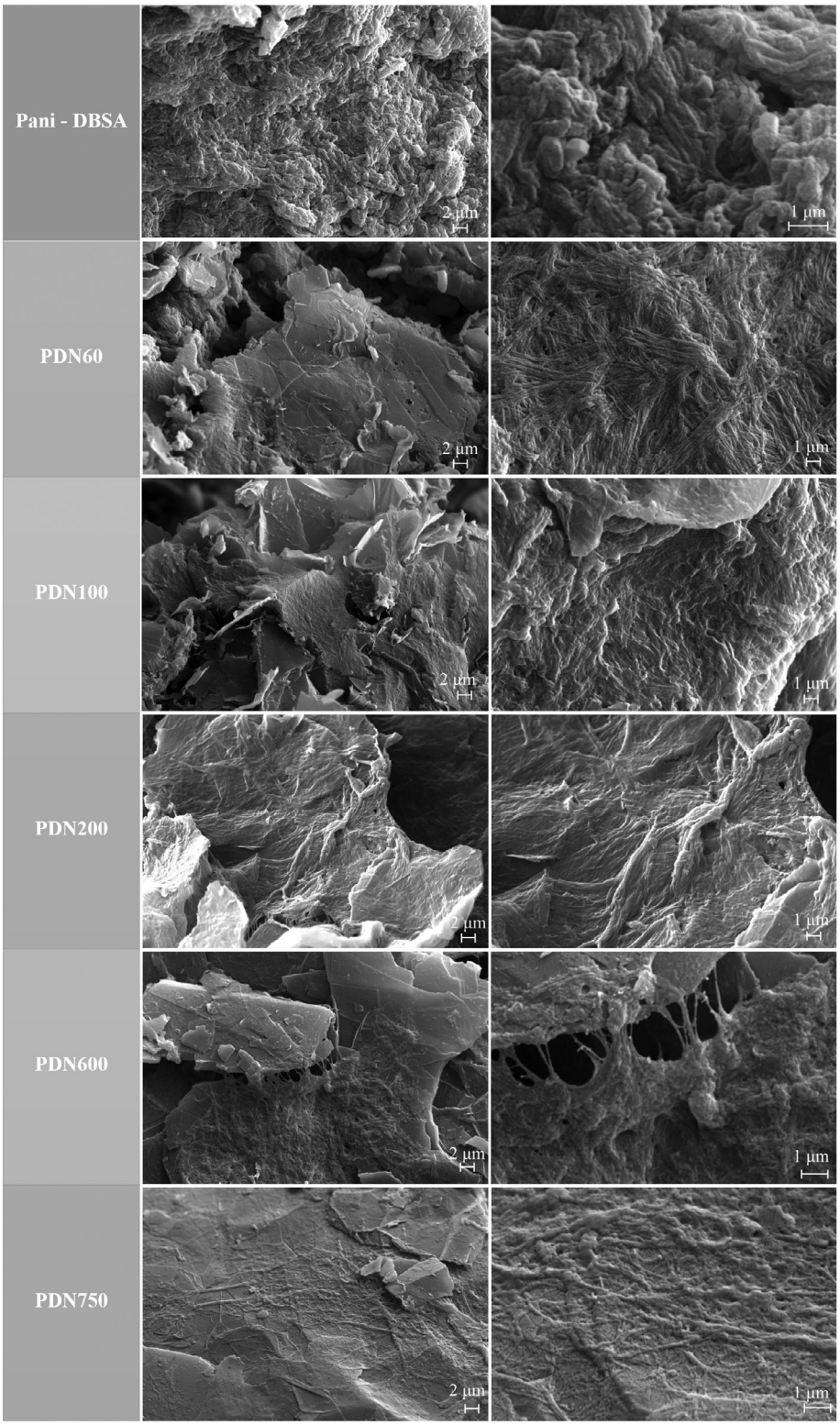

FIGURE 5 SEM micrographs obtained from Pani-DBSA and nanocomposites, focusing on the morphological structure and distribution of Pani-DBSA on the surface of the GNS

intercalation in which the predominant process depends on the synthesis process. In the case of PHN nanocomposites, when mixing monomers with GNS, a limited number of aniline molecules penetrate into the interlayer of the GNS. These confined monomers are then polymerized by the introduction of APS, generating the growth of Pani chains and resulting in the expansion of the GNS planes because of a partial exfoliation process. Such a process can generate structures with a smaller number of stacked graphene layers, or even graphene structures, and can impact electrical conductivity values as discussed in Section 3.5.[74]

On the other hand, in the case of PDN nanocomposites, the interaction of the monomer with the GNS is controlled predominantly by DBSA, which

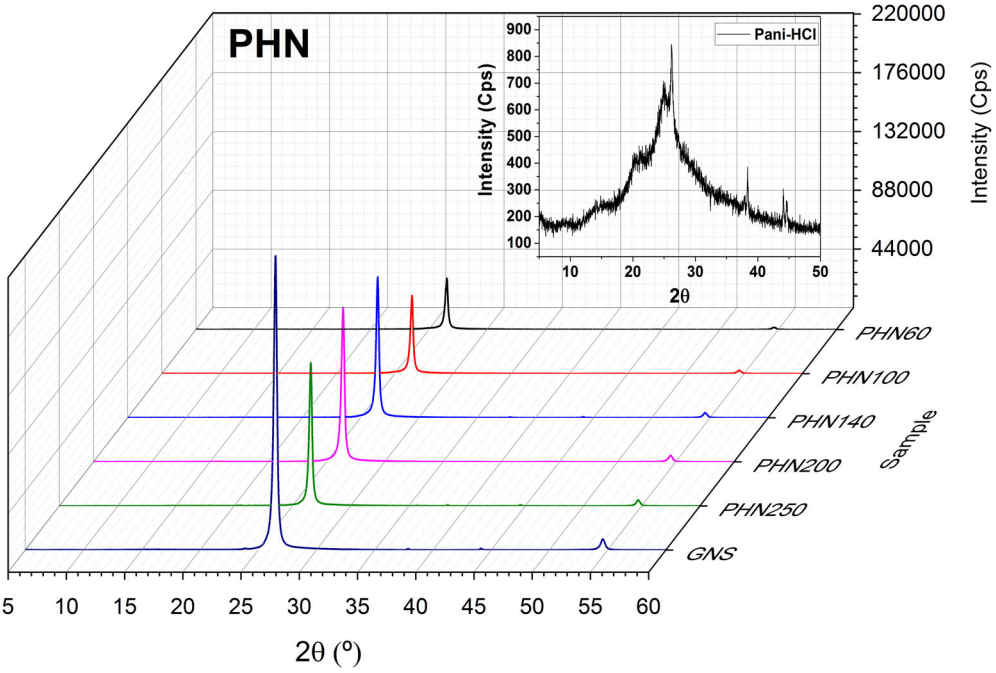

FIGURE 6 X-ray diffraction pattern for Pani-HCl (inset), GNS, and the nanocomposites as a function of GNS concentration in the reaction medium [Color figure can be viewed at wileyonlinelibrary.com]

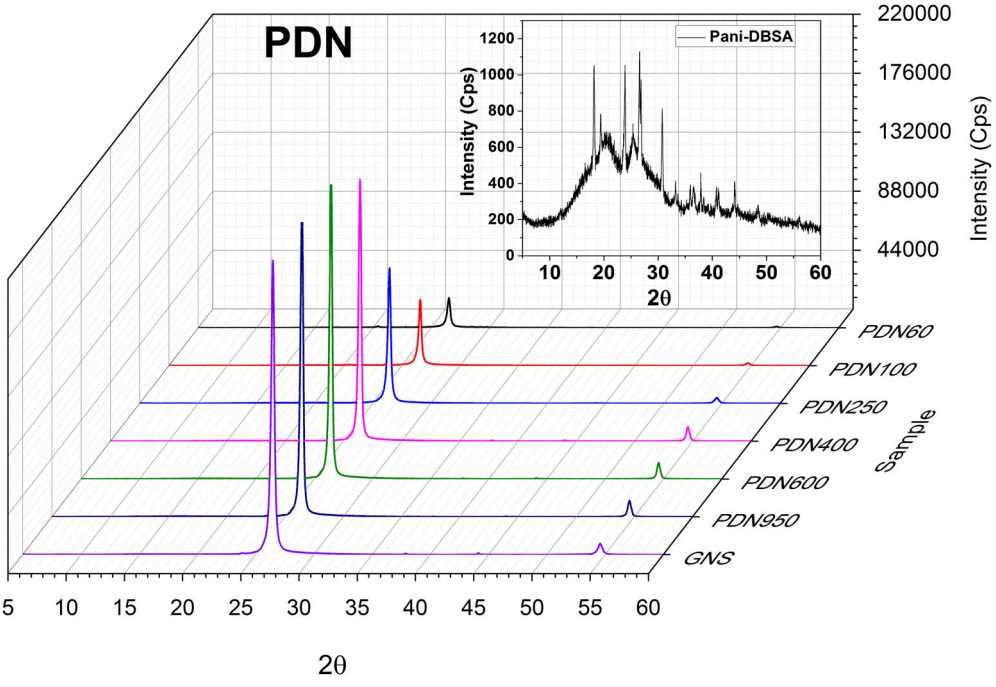

FIGURE 7 X-ray diffraction pattern for Pani-DBSA (inset), GNS, and the nanocomposites as a function of GNS concentration in the reaction medium [Color figure can be viewed at wileyonlinelibrary.com]

limits the process of interposition of aniline molecules between planes. Thus, the increase in the interplanar distance preceded by the increase in the plane intensity (200) observed for the PDN samples is mainly due to the atomic relaxation process resulting from the pseudo-intercalation process,[76,78] which dominates in this case. The reduction in the interplanar distance values after the 400% m/m of GNS fraction for the PDN samples, may be related to the lower coverage and to the increase in the irregularity of the Pani distribution on the surface of the nanoparticles due to the increase in the amount of GNS in the synthesis process that keeps the AN/APS ratio fixed.

3.4 | Thermal analysis—TG/DTG

Figures 9 and 10 illustrates the TG/DTG thermograms for the Pani-HCl and PAni-DBSA samples as well as for their nanocomposites, respectively.

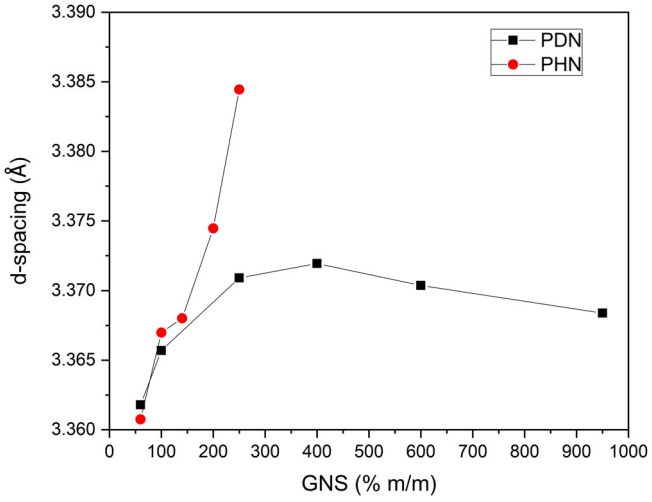

FIGURE 8 Interlayer spacing of the graphite (002) crystal plane as determined from the Bragg equation [Color figure can be viewed at wileyonlinelibrary.com]

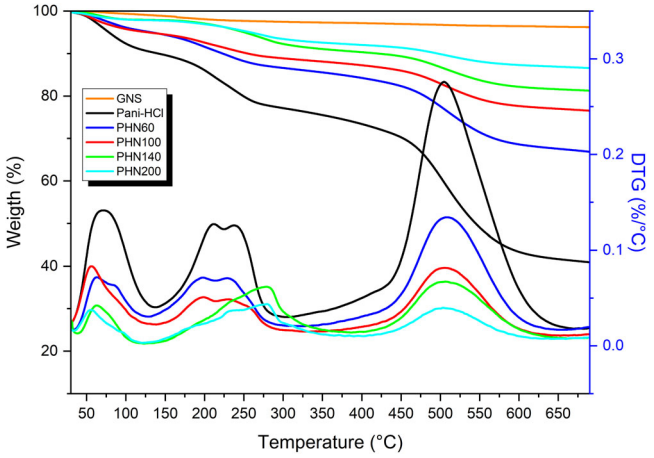

FIGURE 9 Representative TG/DTG curves for Pani-HCl and PHN nanocomposites [Color figure can be viewed at wileyonlinelibrary.com]

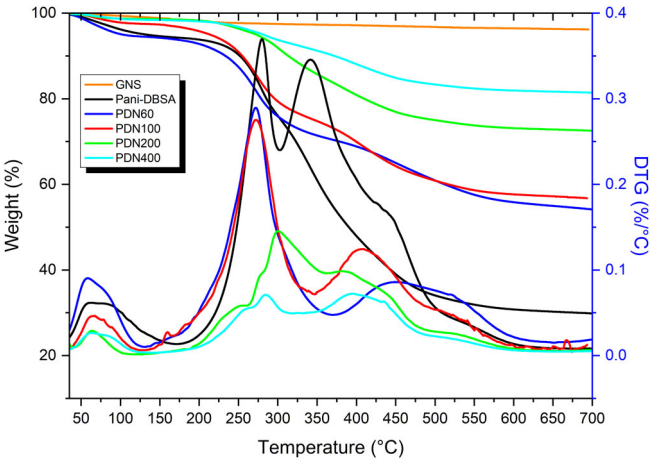

FIGURE 10 Representative TG/DTG curves for PAni-DBSA and PDN nanocomposites [Color figure can be viewed at wileyonlinelibrary.com]

Pani-HCl (Figure 9) showed three stages of mass loss. The first stage at around 30–135°C was attributed to the evaporation of the free dopant and unbound water molecules. The second at around 139–282°C was related to the loss of bound water, the loss of the primary dopant in the form of HCl gas, as well as the loss of oligomers of lower molar mass along the surface of the samples. The third mass loss stage at 420–650°C was correlated to the degradation of fragments of lower molar mass, reticulated chains, and finally, Pani-HCl chains with greater molar mass.[40,49,80]

In turn, Pani-DBSA (Figure 10) presented, in the same way, three main stages of mass loss. The first was located between 40 and 160°C, which was attributed to the loss of adsorbed water and unbound dopant. The second, observed at 182–303°C, was attributed to the loss of —SO_3H functional groups and chemosorbed water. The third stage of mass loss, located between 303 and 500°C, was attributed to the complete degradation of the dopant and the polymeric chain of Pani. Above 500°C, small mass losses were observed, which were associated with carbon residues, such as minerals, metallic impurities, and carbonated polymer fragments.[75,81]

Comparing the Pani-HCl and Pani-DBSA mass loss stages, it can be seen that the greater volume of the counter-ion present in the PAni-DBSA samples resulted in an evaporation of the dopant at a higher temperature than of the Pani-HCl samples. This fact is attributed to the large molecular size and long alkyl group, which tends to get entangled with the Pani chains, thus preventing the DBSA from being volatile at high temperatures.[82]

The GNS did not undergo significant changes in mass over the studied temperature range (loss less than 0.5%), so that their DTG are not illustrated in the thermograms.

Pani-HCl characteristic mass losses were observed in all PHN nanocomposites. However, a substantial displacement of the degradation bands between 139 and 282°C was observed for higher degradation temperatures for samples PHN140 and PHN200. Such behavior was related to the intercalation/pseudo-intercalation process, as evidenced by the X-ray diffraction measurements (Figure 8). The interposition of Pani-HCl between the GNS planes and between the GNS makes it difficult for the dopant to diffuse and evaporate, thus slowing its loss.

The PDN nanocomposite mass loss curves (Figure 10) showed the Pani-DBSA degradation profile, indicating

the presence of the polymer in the samples. As in the PHN nanocomposites, it was found that the dopant degradation processes also shifted to higher temperatures as a result of the predominance of the Pani pseudo-intercalation. The larger size of the counter-ion associated with the pseudo-intercalation process delays the dopant's diffusion, resulting in the widening of the peaks as well as the delay in the degradation process of the main chain, displacing its band at least 50°C in relation to Pani-DBSA. Due to the pseudo-intercalation process as well as the distribution of the GNS in the samples, these behave as a physical barrier to the dopant's migration to external regions. Consequently, the dopant molecules closer to the surface, in an evaporation process, will diffuse more easily and will be released to the external environment more quickly than those located in the innermost regions, causing not only the displacement and widening of the degradation bands of the dopant, as already discussed, but also the presence of shoulders characterized by the release of the dopant in different stages.

3.5 | DC electrical conductivity

Figures 11 and 12 illustrates the behavior of the electrical conductivity of PHN and PDN nanocomposites as a function of GNS content. The GNS showed a conductivity of 759 ± 50 S cm^{-1}, while Pani-HCl and Pani-DBSA showed an electrical conductivity of 20 ± 0.6 and 1.7 ± 0.1 S cm^{-1}, respectively.

The Pani-DBSA showed a lower electrical conductivity than Pani-HCl. The size of the counter-ion affects the electrical conductivity. According to Sinha et al.,[80] the larger size of the dopant exerts more force against ordering and closing of the polymer chains, leading to a lower crystallinity, a higher d-spacing, and a higher interchain separation, which contribute to the decrease in the conductivity. In addition, HCl is a stronger acid than DBSA, which also contributes to a higher conductivity of the Pani-HCl system.

According to percolation theory, a composite's conductivity near the percolation threshold is proportional to the power law (Equations (1) and (*2*)).

$$\sigma \alpha (p - p_c)^t \rightarrow p > p_c \quad (1)$$

$$\sigma \alpha (p_c - p)^{-s} \rightarrow p < p_c \quad (2)$$

where p_c is the percolation threshold, p is the GNS fraction, and t and s are the critical exponents.

PHN and PDN nanocomposites showed different electrical conductivity profiles, as shown in Figures 11 and 12, both discordant of binary disordered systems. The PHN samples exhibited a near linear increasing behavior of the conductivity as a function of GNS content, with a percolation threshold estimated around 100% m/m of GNS (Figure 11). On the other hand, the PDN samples exhibited a multiple percolation profile in which basically two levels were observed, indicating the existence of two distinct percolation thresholds, one at 140% and the other at 325% m/m GNS. Multiple-percolation processes are described in the literature and are linked to local

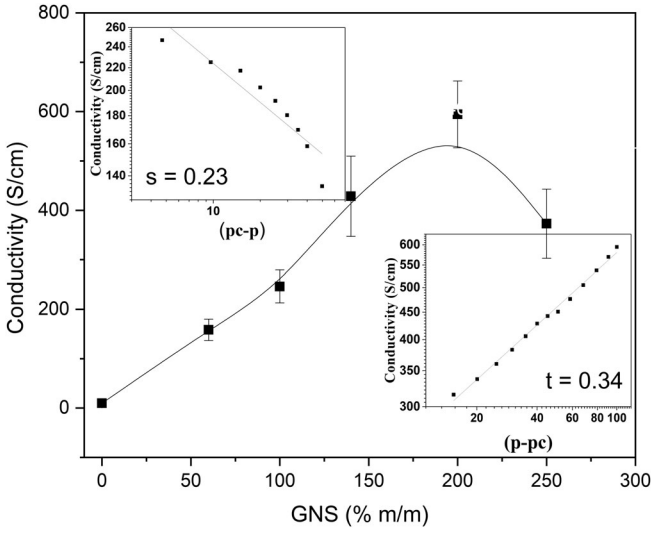

FIGURE 11 DC electrical conductivity as a function of the GNS mass fraction for the PHN nanocomposites. Insets: Fitting obtained for the regions (*pc-p*) and (*p-pc*) and the respective critical exponents

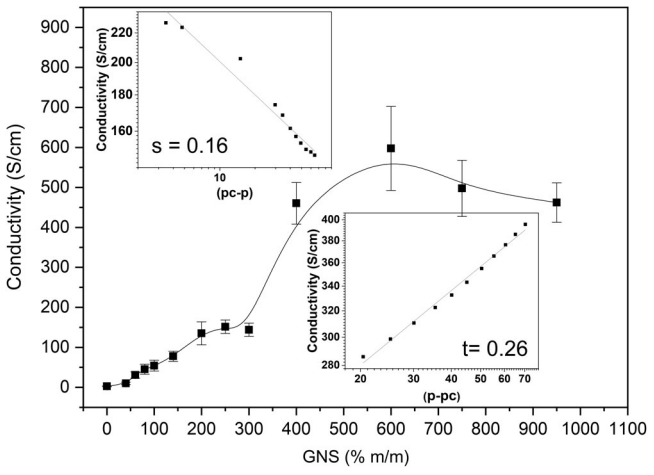

FIGURE 12 DC electrical conductivity as a function of GNS mass fraction for the PDN nanocomposites. Insets: Fitting obtained for the regions (*pc-p*) and (*p-pc*) and the respective critical exponents

variations in concentration and/or shape and orientation of the fill phase, synergistic effects, and electrostatic interactions.[83,84]

The first percolation threshold centered at 140% m/m is related to local variations of the GNS concentration in the samples. This fact demonstrates that, although the GNS coating by Pani-DBSA is higher than that of the PHN samples, a certain irregularity in the GNS distribution in the matrix occurs, as observed in the SEM images. On the other hand, the second percolation threshold, centered at 325% m/m, suggests the percolation of the GNS in the Pani matrix.

The high percolation threshold found for the PDN samples compared to the PHN samples is attributed to the different types of interactions between Pani and GNS during the synthesis process, which results in a lower formation of oligomers in the synthesis process as well as a better coating of the GNS by the Pani-DBSA, as shown in the SEM images. The production of nanostructures with lower stacking, originated in the synthesis process of PHN samples, also contributes to its lower percolation. The insets in Figures 11 and 12 show the fitting obtained for the regions (*pc-p*) and (*p-pc*) and respective critical exponents obtained for each region. It is verified that, below the percolation threshold, the points obtained from the plot show a marked dispersion for both PHN and PDN samples, moving away from the power law (Equation (1)).

The increase in conductivity for both nanocomposites below the percolation threshold is due to the high mobility of the charge carriers in the GNS. These act as bridges through the π–π interactions between the Pani and the GNS structure, facilitating the transport of the charge carriers between the PANI chains[85–87] and promoting an initial conductivity increase of approximately 16 times compared to Pani for the PHN nanocomposites and 60 times for the PDN nanocomposites at 60% m/m GNS content.

These interactions, together with the irregularity of the Pani coating, in both nanocomposites directly generate the distortion of the critical exponents. This suggests a possible increase in the density of interactions between the Pani matrix and the structure of the GNS resulting from the increase in the contact area of Pani with the GNS through a possible pseudo-intercalation process and exfoliation. Thus, the electrical conductivity reductions above 600% GNS for PDN samples, among other factors mentioned above, are related to the saturation of the Pani interposition processes as well as reductions in the crystallinity values of the GNS, as verified by the X-ray diffraction pattern.

Above the percolation threshold, there is a predominance of electrical conduction processes between GNS-GNS, and the nanocomposites reach conductivity values close to the electrical conductivity of the GNS. This factor leads to a "better behaved" profile for the plotted points, as shown in the region-related (*p-pc*) insets presented for both samples. However, the critical exponent for such a region is not accordance with those expected by classical percolation theory. Above the percolation, as the amount of GNS increases, phase inversion begins with the predominance of GNS as a matrix. As a consequence, the coating and distribution of Pani become more irregular, and the presence of oligomers, such as phenazine units, increases, thus acting as resistance bridges. This fact is evidenced mainly by the irregular behavior of the statistical deviation distribution, which increases with increasing GNS content mainly above the percolation threshold, a fact that is anomalous for percolative systems based on conductive phases.[88,89] This suggests that the values found for conductivity are linked not only to specific interactions of Pani with GNS, but also to distinct conduction processes that vary according to the distribution and association of nanosheets, uncoated or coated with Pani, promoting local variations in the conductivity of the samples.

4 | CONCLUSION

GNS/Pani nanocomposites were produced by in situ polymerization of aniline in the presence of GNS using HCl and DBSA as dopants. In the nanocomposite, the Pani-HCl changed the globular morphology (neat Pani) to a rod-like morphology, while the Pani-DBSA showed longer and more organized nanofibrils than Pani–DBSA. These structural morphology changes are related to the different processes of anchorage that occurred during the syntheses. An increase in the interplanar spacing of the GNS promoted by the presence of Pani was observed and its dependence on the type of dopant employed was demonstrated. This process was correlated with the hybrid existence of an intercalation/pseudo-intercalation process whose prevalence depends on the type of dopant and the general characteristics of the synthesized Pani. Such factors influence the thermal stability of the nanocomposites by promoting an increase in the Pani degradation temperature to 50°C. The electrical conductivity of the nanocomposites did not follow the universal law. This fact was attributed to the interaction between Pani and GNS that resulted in a distortion of the critical exponents. The PDN DC electrical conductivity showed a double percolation. The first one (140 m/m %) was attributed to the irregular coating of Pani-DBSA in the GNS, and the second one (325 m/m %) was associated with the matrix inversion. Prominent applications of these multifunctional nanocomposites include gas sensors, pH,

chemical sensors, electromagnetic shielding, etc. However, considering the intercalation/pseudo-intercalation behavior, highlighted in this study, a new application of these materials emerges in the sensing and control of temperatures promoted by the barrier effect of GNS on conductivity and that should be further investigated.

ACKNOWLEDGMENT

The authors express their gratitude to Fundação de Amparo à Pesquisa do Estado de São Paulo – FAPESP (CEPID – CDMF Grant N° 2013/07296-2), Coordenação de Aperfeiçoamento de Pessoal de Nível Superior – CAPES (Finance Code 001) and Conselho Nacional de Desenvolvimento Científico e Tecnológico (CNPq) (Grant N° 309249/2015-5), for their financial support and scholarship.

AUTHOR CONTRIBUTIONS

Eliza Sbrogio Martin: Conceptualization (equal); data curation (lead); formal analysis (lead); investigation (lead); methodology (lead); validation (equal); writing – original draft (equal). **Alex Otávio Sanches:** Conceptualization (equal); formal analysis (equal); methodology (equal); writing – original draft (equal); writing – review and editing (equal). **Thuany Garcia Maraschin:** Conceptualization (supporting); formal analysis (supporting); methodology (equal); resources (equal); validation (supporting); writing – original draft (supporting); writing – review and editing (supporting). **Nara Regina de Souza Basso:** Conceptualization (supporting); formal analysis (equal); funding acquisition (equal); investigation (supporting); methodology (supporting); project administration (equal); resources (equal); writing – original draft (equal); writing – review and editing (supporting). **Fernando Rogério de Paula:** Formal analysis (supporting); investigation (supporting); writing – original draft (supporting); writing – review and editing (supporting).

DATA AVAILABILITY STATEMENT

Research data are not shared.

ORCID

Alex Otávio Sanches https://orcid.org/0000-0003-2730-7435

REFERENCES

[1] Y. Luo, R. Guo, T. Li, F. Li, Z. Liu, M. Zheng, B. Wang, Z. Yang, H. Luo, Y. Wan, *ChemSusChem* **2019**, *12*, 1591.
[2] H. Liu, R. Jing, C. You, Q. Zhong, *MRS Commun.* **2019**, *9*, 1355.
[3] G. C. Li, G. R. Li, S. H. Ye, X. P. Gao, *Adv. Energy Mater.* **2012**, *2*, 1238.
[4] H. Deng, L. Yao, Q. A. Huang, Q. Su, J. Zhang, F. Zhang, G. Du, *RSC Adv.* **2017**, *7*, 9819.
[5] Z. Wang, J. J. Han, N. Zhang, D. D. Sun, T. Han, *J. Solid State Electrochem.* **2019**, *23*, 3373.
[6] D. D. L. Chung, *Mater. Chem. Phys.* **2020**, *255*, 123587.
[7] K. Zubair, A. Ashraf, H. Gulzar, M. F. Shakir, Y. Nawab, Z. A. Rehan, I. A. Rashid, *Nano Express* **2021**, *2*, 010038.
[8] R. Manna, S. K. Srivastava, *ACS Omega* **2021**, *6*, 9164.
[9] F. Zhang, W. Cui, B. Wang, B. Xu, X. Liu, X. Liu, Z. Jia, G. Wu, *Composites, Part B* **2021**, *204*, 108491.
[10] J. M. Sansiñena, J. Gao, H. L. Wang, *Adv. Funct. Mater.* **2003**, *13*, 703.
[11] S. Yun, J. Kim, *J. Phys. D: Appl. Phys.* **2006**, *39*, 2580.
[12] M. Weng, Y. Duan, P. Zhou, F. Huang, W. Zhang, L. Chen, *Nano Energy* **2020**, *68*, 104365.
[13] W. Li, C. L. Johnson, H. L. Wang, *Polymer* **2004**, *45*, 4769.
[14] Z. Li, L. Gong, *Materials* **2020**, *13*, 548.
[15] P. Flouda, A. H. Quinn, A. G. Patel, D. Loufakis, D. C. Lagoudas, J. L. Lutkenhaus, *Nanoscale* **2020**, *12*, 16840.
[16] H. Wang, J. Lin, Z. X. Shen, *J. Sci. Adv. Mater. Devices* **2016**, *1*, 225.
[17] O. Sadak, M. U. A. Prathap, S. Gunasekaran, *Carbon* **2019**, *144*, 756.
[18] H. Lyu, *Polymer* **2020**, *12*, 49.
[19] A. Ramadan, M. Anas, S. Ebrahim, M. Soliman, A. I. Abou-Aly, *Int. J. Hydrogen Energy* **2020**, *45*, 16254.
[20] J. Diao, J. Yuan, A. Ding, J. Zheng, Z. Lu, *Macromol. Mater. Eng.* **2018**, *303*, 1.
[21] S. Ke, T. Ouyang, K. Zhang, Y. Nong, Y. Mo, Q. Mo, Y. Wei, F. Cheng, *Macromol. Mater. Eng.* **2019**, *304*, 1.
[22] M. Mozafari, N. Pal Singh Chauhan Eds., *Fundamentals and Emerging Applications of Polyaniline*, Elsevier, Amsterdam **2019**.
[23] C. Bavatharani, E. Muthusankar, S. M. Wabaidur, Z. A. Alothman, K. M. Alsheetan, M. m. AL-Anazy, D. Ragupathy, *Synth. Met.* **2021**, *271*, 116609.
[24] J. Bhadra, A. Alkareem, N. Al-Thani, *J. Polym. Res.* **2020**, *21*, 116609.
[25] C. I. Idumah, *Synth. Met.* **2021**, *273*, 116674.
[26] C. U. Seo, Y. Yoon, D. H. Kim, S. Y. Choi, W. K. Park, J. S. Yoo, B. Baek, S. B. Kwon, C. M. Yang, Y. H. Song, D. H. Yoon, W. S. Yang, *J. Ind. Eng. Chem.* **2018**, *64*, 97.
[27] S. A. Akbar, *J. Phys.: Conf. Ser.* **2019**, *1232*, 1.
[28] J. Wu, Y. Zou, X. Li, H. Liu, G. Shen, R. Yu, *Sens. Actuators, B* **2005**, *104*, 43.
[29] S. P. Gumfekar, W. Wang, B. Zhao, *Macromol. Mater. Eng.* **2014**, *299*, 966.
[30] F. R. Simões, L. O. S. Bulhões, E. C. Pereira, *Polimeros* **2009**, *19*, 54.
[31] L. M. G. da Silva, H. G. Lemos, S. F. Santos, R. A. Antunes, E. C. Venancio, *Mater. Today Commun.* **2018**, *16*, 14.
[32] N. M. Thong, Q. V. Vo, T. Le Huyen, M. Van Bay, N. N. Dung, P. T. Thu Thao, P. C. Nam, *RSC Adv.* **2020**, *10*, 14595.
[33] J. C. Wu, S. S. Chen, T. C. Yu, K. C. W. Wu, C. H. Hou, *Sep. Purif. Technol.* **2021**, *254*, 117561.
[34] O. Gorduk, M. Gencten, S. Gorduk, M. Sahin, Y. Sahin, *J. Energy Storage* **2021**, *33*, 102049.
[35] P. Najmi, N. Keshmiri, M. Ramezanzadeh, B. Ramezanzadeh, *J. Taiwan Inst. Chem. Eng.* **2021**, *119*, 245.

[36] S. E. Bourdo, T. Viswanathan, *Carbon* **2005**, *43*, 2983.
[37] X. Wu, S. Qi, J. He, B. Chen, G. Duan, *J. Polym. Res.* **2010**, *17*, 751.
[38] X. Wu, S. Qi, G. Duan, *Synth. Met.* **2012**, *162*, 1609.
[39] Y. Li, X. Zhao, P. Yu, Q. Zhang, *Langmuir* **2013**, *29*, 493.
[40] G. Gheno, N. R. De Souza Basso, R. Hübler, *Macromol. Symp.* **2011**, *299–300*, 74.
[41] Z. Mo, H. Shi, H. Chen, G. Niu, Z. Zhao, Y. Wu, *J. Appl. Polym. Sci.* **2009**, *112*, 573.
[42] S. M. Firdaus, A. S. Anasyida, S. A. Zubir, M. Mariatti, *J. Mater. Sci.: Mater. Electron.* **2020**, *31*, 15805.
[43] J. Stejskal, I. Sapurina, M. Trchová, *Progr. Polym. Sci. (Oxford)* **2010**, *35*, 1420.
[44] F. D. C. Fim, J. M. Guterres, N. R. S. Basso, G. B. Galland, *J. Polym. Sci. Part A Polym. Chem.* **2010**, *48*, 692.
[45] G. Bharath, E. Alhseinat, N. Ponpandian, M. A. Khan, M. R. Siddiqui, F. Ahmed, E. H. Alsharaeh, *Sep. Purif. Technol.* **2017**, *188*, 206.
[46] R. Miraftab, B. Karimi, G. Bahlakeh, B. Ramezanzadeh, *J. Ind. Eng. Chem.* **2017**, *53*, 348.
[47] S. Bhadra, D. Khastgir, *Polym. Degrad. Stab.* **2008**, *93*, 1094.
[48] Y. Zhao, G. S. Tang, Z. Z. Yu, J. S. Qi, *Carbon* **2012**, *50*, 3064.
[49] M. O. Ansari, S. K. Yadav, J. W. Cho, F. Mohammad, *Composites, Part B* **2013**, *47*, 155.
[50] J. Prokeš, M. Trchová, D. Hlavatá, J. Stejskal, *Polym. Degrad. Stab.* **2002**, *78*, 393.
[51] M. Trchová, I. Šeděnková, E. Tobolková, J. Stejskal, *Polym. Degrad. Stab.* **2004**, *86*, 179.
[52] S. Quillard, G. Louarn, J. P. Buisson, M. Boyer, M. Lapkowski, A. Pron, S. Lefrant, *Synth. Met.* **1997**, *84*, 805.
[53] H. Zengin, W. Zhou, J. Jin, R. Czerw, D. W. Smith, L. Echegoyen, D. L. Carroll, S. H. Foulger, J. Ballato, *Adv. Mater.* **2002**, *14*, 1480.
[54] Y. Yu, B. Che, Z. Si, L. Li, W. Chen, G. Xue, *Synth. Met.* **2005**, *150*, 271.
[55] W. Li-Xiang, J. Xia-Bin, W. Fo-Song, *Acta Chim. Sin. Engl. Ed.* **1989**, *7*, 53.
[56] A. T. Hidayat, A. Kusumaatmaja, Chotimah, R. Soekrisno, K. Triyana, *AIP Conf. Proc.* **2016**, *1755*, 150015.
[57] M. A. C. Mazzeu, L. K. Faria, M. R. Baldan, M. C. Rezende, E. S. Gonçalves, *Braz. J. Chem. Eng.* **2018**, *35*, 123.
[58] P. Pawar, A. B. Gaikawad, P. P. Patil, *Sci. Technol. Adv. Mater.* **2006**, *7*, 732.
[59] M. Trchová, J. Stejskal, *Pure Appl. Chem.* **1803**, *2011*, 83.
[60] Y. Furukawa, F. Ueda, Y. Hyodo, I. Harada, T. Nakajima, T. Kawagoe, *Macromolecules* **1988**, *21*, 1297.
[61] I. Harada, Y. Furukawa, F. Ueda, *Synth. Met.* **1989**, *29*, 303.
[62] D. S. Vicentini, R. V. Salvatierra, A. J. G. Zarbin, L. G. Dutrac, M. M. Sá, *J. Braz. Chem. Soc.* **1939**, *2014*, 25.
[63] J. Stejskal, I. Sapurina, M. Trchová, E. N. Konyushenko, P. Holler, *Polymer* **2006**, *47*, 8253.
[64] M. G. Han, S. K. Cho, S. G. Oh, S. S. Im, *Synth. Met.* **2002**, *126*, 53.
[65] O. Misoon, K. Seok, *Electrochim. Acta* **2012**, *59*, 196.
[66] D. Han, Y. Chu, L. Yang, Y. Liu, Z. Lv, *Colloids Surf., A* **2005**, *259*, 179.
[67] Y. Wang, A. Liu, T. Li, Y. Han, Y. Ma, Q. Zhang, J. Zhang, *J. Electron. Mater.* **2020**, *49*, 3751.
[68] R. Kumar, M. O. Ansari, M. A. Barakat, *Chem. Eng. J.* **2013**, *228*, 748.
[69] N. M. Barkoula, B. Alcock, N. O. Cabrera, T. Peijs, *Polym. Polym. Compos.* **2008**, *16*, 101.
[70] O. E. Andersson, B. L. V. Prasad, H. Sato, T. Enoki, Y. Hishiyama, Y. Kaburagi, M. Yoshikawa, S. Bandow, *Phys. Rev. B* **1998**, *58*, 16387.
[71] N. T. Tung, T. Van Khai, H. Lee, D. Sohn, *Synth. Met.* **2011**, *161*, 177.
[72] S. Bhandari, N. K. Singha, D. Khastgir, *J. Appl. Polym. Sci.* **2013**, *129*, 1264.
[73] Y. Guo, F. Peng, H. Wang, F. Huang, F. Meng, D. Hui, Z. Zhou, *Polymer* **2018**, *10*, 1.
[74] X. Chen, F. Meng, Z. Zhou, X. Tian, L. Shan, S. Zhu, X. Xu, M. Jiang, L. Wang, D. Hui, Y. Wang, J. Lu, J. Gou, *Nanoscale* **2014**, *6*, 8140.
[75] P. Saini, V. Choudhary, K. N. Sood, S. K. Dhawan, *J. Appl. Polym. Sci.* **2009**, *113*, 3146.
[76] S. E. Bourdo, B. A. Warford, T. Viswanathan, *J. Solid State Chem.* **2012**, *196*, 309.
[77] T. N. Atiqah, S. J. Tan, K. L. Foo, A. G. Supri, A. M. M. Al Bakri, Y. M. Liew, *Polym. Bull.* **2018**, *75*, 209.
[78] S. Bourdo, Z. Li, A. S. Biris, F. Watanabe, T. Viswanathan, I. Pavel, *Adv. Funct. Mater.* **2008**, *18*, 432.
[79] Z. Q. Li, C. J. Lu, Z. P. Xia, Y. Zhou, Z. Luo, *Carbon* **2007**, *45*, 1686.
[80] S. Sinha, S. Bhadra, D. Khastgir, *J. Appl. Polym. Sci.* **2009**, *112*, 3135.
[81] C. Basavaraja, W. J. Kim, D. G. Kim, D. S. Huh, *Polym. Compos.* **2012**, *33*, 388.
[82] T. Chen, C. Dong, X. Li, J. Gao, *Polym. Degrad. Stab.* **2009**, *94*, 1788.
[83] D. H. McQueen, K. M. Jäger, M. Pelíšková, *J. Phys. D: Appl. Phys.* **2004**, *37*, 2160.
[84] A. O. Sanches, D. H. F. Kanda, L. F. Malmonge, M. J. da Silva, W. K. Sakamoto, J. A. Malmonge, *Polym. Test.* **2017**, *60*, 253.
[85] X. S. Du, M. Xiao, Y. Z. Meng, *Eur. Polym. J.* **2004**, *40*, 1489.
[86] C. Xiang, L. Li, S. Jin, B. Zhang, H. Qian, G. Tong, *Mater. Lett.* **2010**, *64*, 1313.
[87] E. Cokun, E. A. Zaragoza-Contreras, H. J. Salavagione, *Carbon* **2012**, *50*, 2235.
[88] R. Hashemi, G. J. Weng, *Carbon* **2016**, *96*, 474.
[89] J. Fournier, G. Boiteux, G. Seytre, G. Marichy, *Synth. Met.* **1997**, *84*, 839.

How to cite this article: E. S. Martin, A. O. Sanches, T. G. Maraschin, N. R. de Souza Basso, F. R. de Paula, J. A. Malmonge, *J. Appl. Polym. Sci.* **2022**, *139*(22), e52363. https://doi.org/10.1002/app.52363